Effect of 16 O 6+ ion-irradiation on structural, magnetic properties and antistructural modeling of Zn-nanoferrites

C. Parmar, R. Verma, S S Modak, Frédéric Mazaleyrat, Tetiana Tatarchuk, S N Kane

Effect of $^{16}O^{6+}$ ion-irradiation on structural, magnetic properties and antistructural modeling of Zn-nanoferrites

C. Parmar [1], R. Verma[1], S. S. Modak [2], F. Mazaleyrat [3], Tetiana Tatarchuk [4,*], S. N. Kane[1,#]

[1] School of Physics, D. A. University, Khandwa Road, Indore, 452001, India

[2] Physics Department, Jaypee University of Eng. and Tech., Guna 473226, India

[3] SATIE, ENS Paris-Saclay, 4 Av. Des Sciences, 91190 Gif-sur-Yvette, France

[4] Educational and Scientific Center of Materials Science and Nanotechnology, Vasyl Stefanyk Precarpathian National University, Ivano-Frankivsk, 76015, Ukraine

*Corresponding author: tatarchuk.tetyana@gmail.com

e mail: kane_sn@yahoo.com

Abstract

XRD analysis and magnetic measurements were used to study the effect of 80 MeV $^{16}O^{6+}$ ion-irradiation on structural, magnetic properties, and anti-structural modeling of as-burnt $ZnFe_2O_4$ synthesized by sol-gel auto-combustion technique. XRD confirms the formation of single-phase spinel nanoferrite. Irradiation leads to modification of i) lattice-parameter; strain; oxygen parameter, Fe^{3+}, Zn^{2+}ions on A, B site; inversion degree; A-O-B, A-O-A, B–O–B super-exchange-interaction; ii) saturation magnetization; anisotropy; squareness-ratio; surface dead-layer-thickness. Antistructural modeling describes the surface-active centers for pristine and irradiated samples. Studies reveal strong connection between structural and magnetic properties, useful for ion-irradiation-induced tuning properties of $ZnFe_2O_4$.

Keywords: *Spinel ferrite; Sol-gel auto-combustion; Ion-irradiation; Magnetic measurements; Cationic distribution.*

1. Introduction

Ferrimagnetic spinel ferrites with general formula $M^{2+}Fe^{3+}{}_2O_4$, display face-centered cubic fcc structure, Fd3m space group, and have two inter-penetrating sub lattices tetrahedral (A), octahedral (B) [1]. Structural modification of spinel ferrites brings assorted properties suitable for a wide range of applications including those in the microwave; spintronic devices, drug delivery, computer memories, bio-sensing, space application, in a radioactive environment, and Magnetic Resonance Imaging, etc. [2, 3, 4, 5].

Swift heavy ion (SHI) irradiation is a novel technique, used for structural modification [6], and can be employed to study the variation of structural and magnetic properties of materials [7, 8, 9, 10]. When ions pass through a material, they pass on their momentum, energy to the material, and depending on the energy of ions two regimes can be defined: via nuclear energy regime (few keV), and electronic energy regime (> few MeV). Tailoring structural, magnetic properties of spinel ferrites by SHI is a work of quite a significance, as it not only increases the applicability of spinel ferrites e. g. in photocatalytic materials for renewable energy [11], but also elucidates the interaction of swift heavy ions with magnetic nanomaterials. Studies [12] also describe the SHI irradiation-induced generation of defects in metal oxides resulting in the modifications on the surface of the nanoparticles which leads to noticeable changes in the structural and physical properties. It is well recognized that changes in the properties of materials are immensely affected by the type of ion beam; its energy, and the material composition [13]. Although literature reports SHI irradiation-induced modification of structural and magnetic properties Co-Zn, Mn-Zn, Ni-Zn, $ZnFe_2O_4$, $NiFe_2O_4$ ferrites [14, 15, 16, 17, 18, 19, 20], it infrequently reports the effect of irradiation on the antistructural modeling to describe surface active centers, the correlation between structural, cationic distribution, and magnetic properties of Zn ferrite [20].

Thus, the current work aims to study the effect of 80 MeV $^{16}O^{6+}$ ion-irradiation on structural, magnetic properties, anti-structural modeling of as-burnt $ZnFe_2O_4$ synthesized by sol-gel auto-combustion technique, monitored by XRD, and magnetic measurements.

2. Material synthesis, material characterization, and data analysis

$ZnFe_2O_4$ was synthesized utilizing AR grade citrate-nitrate precursors: [*Zinc Nitrate* – [($Zn(NO_3)_2.6H_2O$, *Ferric Nitrate* – $Fe(NO_3)_3 \cdot 9H_2O$ and *Citric acid* - $C_6H_8O_7$] by sol-gel auto combustion method. All the precursors were taken in stoichiometric ratio and were mixed in 10 ml de-ionized water, and pH 7 was maintained by adding ammonia (NH_4OH) solution. The obtained clear solution was then heated at ~115 ºC in the air to obtain the fluffy powder, called '*dry gel*'.

Prepared $ZnFe_2O_4$ sample was irradiated with 80 MeV $^{16}O^{6+}$ ion at a flounce of 1×10^{11}, 1×10^{12}, 1×10^{13} ions/cm^2 by using 15 UD Pelletron Accelerator at Inter-University Accelerator Centre 'IUAC', New Delhi (INDIA). Un-irradiated and irradiated $ZnFe_2O_4$ samples were used for structural, and magnetic characterization.

SRIM (*The Stopping and Range of Ions in Matter*) code [21] was used to calculate the penetration depth of ion (R_P), nuclear energy loss (S_n), and electronic energy loss (S_e) using density: *5402.44 kg/m^3* in $ZnFe_2O_4$. For 80 MeV $^{16}O^{6+}$ ion irradiation of $ZnFe_2O_4$ computed S_e: 164.6 eV/Å, and S_n: is 0.0995 eV/Å with R_P 35.72 μm. It is worth noting that the observed electronic energy loss (S_e) is more than the nuclear energy loss (S_n) for 80 MeV $^{16}O^{6+}$ ion irradiation, indicating that S_e is the dominant process, which produces the structural modification in the material. To avoid ion implantation, sample thickness was selected such that it is less than R_P, thus ions will pass through the sample.

Room temperature X-ray diffraction (XRD) measurements (*$\theta - 2\theta$ configuration*) were done by using Bruker D8 advance diffractometer utilizing Cu-K_α radiation (λ= 0.154056 nm). Room temperature hysteresis loops were obtained using a vibrating sample magnetometer 'VSM', (*Model: Lakeshore Model 7410*) by applying a maximum applied field: $H_{max.} = \pm 1.9 \times 10^4$ *Oe.*

Rietveld refinement software MAUD (***M**aterial **A**nalysis **U**sing **D**iffraction*) [22] was employed to obtain a Full profile analysis of XRD patterns that confirmed the formation of a single cubic spinel phase, no other phases were detected.

XRD data were analyzed to compute structural parameters: experimental lattice parameter ($a_{exp.}$), cell volume (V), and X-ray density (ρ_{xrd}) as described in [16, 23]. By using Williamson-Hall (W-H) method, grain diameter ($D_{W\text{-}H}$) was obtained by incorporating both instrumental and strain broadening [16, 24]. The XRD data of the standard LaB_6 sample was used to obtain instrumental broadening. By using this method, x-ray diffraction peak broadening is given by the following expression: $\beta_{hkl} = \beta_{size} + \beta_{strain}$. The actual peak broadening (β) is obtained by correcting the experimental peak broadening 'β_{ex}' and the instrumental broadening 'β_{in}' as: $\beta^2 = \beta_{ex}^2 - \beta_{in}^2$. Consequently, the modified form of XRD peak broadening $\beta_{hkl} = \beta_{size} + \beta_{strain}$ equation [16, 24] can be given as:

$$\beta_{hkl} = (0.94\lambda / D_{W\text{-}H}\cos\theta) + 4\varepsilon\tan\theta$$

and

$$\beta_{hkl\cos\theta} = (0.94\lambda / D_{W\text{-}H}) + 4\varepsilon\sin\theta \quad (1)$$

where λ is the wavelength of the X-ray used, β is full width at half maximum (*FWHM*), $D_{W\text{-}H}$ is Williamson-Hall grain diameter, and ε is a strain.

Dislocation density (ρ_D) was calculated by using the following expression [25]:

$$\rho_D = 15\varepsilon / a_{exp.} \times D_{W-H} \quad (2)$$

where a_{exp} is the lattice parameter, $D_{W\text{-}H}$ is Williamson-Hall grain diameter, and ε is a strain.

Cationic distribution was estimated by XRD peak intensities employing Bertaut method [26]. It gives cationic distribution by matching the computed, experimental ratios of intensity for: (422), (400), and (220) planes as described in [27]. For dissimilar cation distribution on A and B sites, intensity ratio: I(400)/I(422), I(220)/I(400) varies. The best cation distribution amongst the A and B sites for which theoretical, experimental ratios ($I_{hkl}^{Obs.}$ and $I_{hkl}^{Cal.}$) of the observed, and calculated intensities agree noticeably, is taken to be the right one. Obtained cationic distribution was used to

calculate theoretical magnetization at 0 K: '$M_{s(th)}$' (also known as Néel magnetic moment 'n_N'). By utilizing the cationic distribution, oxygen position parameter (u), Inversion parameter (δ), and bond angles (θ_1, θ_2, θ_3, θ_4, θ_5), canting angle $\alpha_{Y\text{-}K}$ were calculated as described in [16, 23]. The bulk saturation magnetization (M_B), and magnetic dead layer thickness (t) were computed as described in [16, 20, 28]. As magnetization curves are not saturated, but are in approach to saturation region, the saturation magnetization 'M_s' values were obtained by plotting magnetization 'M' versus 1/H (magnetic field), and linear fit was obtained with extrapolation to zero, where curve intersects the y-axis, is taken as saturation magnetization *'M_s'*, as was also reported in [16]. The coercivity (H_c), and remanence (M_r) are obtained from hysteresis loops. Anisotropy constant (K_1) was calculated by using the equation described in [23]:

$$K_1 = [H_c \times M_s] / 0.96 \quad (3)$$

where M_s is a saturation magnetization, and H_c is a coercivity.

The errors shown in Tables and Figures are the Standard Deviation obtained from the data.

3. Results and Discussions

XRD patterns of pristine and irradiated $ZnFe_2O_4$ samples are shown in Figure 1(a), confirming the formation of a single-phase cubic spinel structure. Inset of Figure 1 (a) shows the expanded view of (311) peak. Figure 1(b) depicts the reduction of $a_{exp.}$ with irradiation dose, indicates irradiation-induced shrinkage of spinel unit cell, described by experimental relation: $a_{exp.} = 0.8401+0.0025[Irr.\ dose]-0.0007\ [Irr.\ dose]^2$, showing strong correlation between irradiation dose and $a_{exp.}$, while the inset of Figure 2 (b) depicts irradiation dose dependence of ρ_{XRD} (right), and ρ_D (left) are consistent with observed changes in a_{exp}, shown in Table 1 along with other XRD parameters.

Fig. 1.

Figure 2 depicts the Rietveld refined XRD patterns, and Table 1 gives the refined R; shape parameters (u, v,w). A representative W–H plot for the pristine and irradiated samples (*dose: 1×10^{11} ions/cm^2*) is shown in Figure 3 (a, b).

Fig. 2.

Fig. 3.

Table 1.

Table 2 depicts experimental, theoretical lattice parameter ($a_{exp.}$, $a_{th.}$), Willimson–Hall (W-H) grain diameter (D_{W-H}), x-ray density, specific surface area (S), strain, and dislocation density. A perusal of Table 1 shows that the observed variation of S is consistent with obtained D_{W-H} and ρ_{XRD} values, and higher S values are useful in heterogeneous catalysis as is also reported earlier [20].

Table 2.

Table 3 depicts the cationic distribution, oxygen parameter u, inversion parameter δ, canting angle 'α_{Y-K}' and intensity ratios of $\mathbf{I_{400}/I_{422}}$, $\mathbf{I_{220}/I_{440}}$. A perusal of Table 3 shows that ion irradiation results in cationic redistribution, as was also reported earlier [15, 16, 17]. Ion irradiation leads to the reduction of Fe^{3+} ions on B-site with simultaneous increase on the A-site, while Zn^{2+} ions remain more populated on the A-site than on the B-site, obtained from cationic distribution. Rather close agreement of $a_{exp.}$, $a_{th.}$ (see Table 1), and intensity ratios of $\mathbf{I_{400}/I_{422}}$, $\mathbf{I_{220}/I_{440}}$ (see Table 3) reveal that the cation distribution on A and B-site (see Table 3) is close to reality [17]. Ion irradiation induced strain reduction is also reflected in decrease of oxygen positional parameter 'u' (see table 3). Ion irradiation mediated changes in cationic distribution also results in increase of inversion degree from 0.15 to 0.30. The perusal of Table 3 also depicts canting angle values, and finite α_{Y-K} values show the applicability of the Yafet-Kittel three sub-lattice model [29] to describe magnetic properties. Table 3 shows ion irradiation prompted changes in u (*range between: 0.3836 – 0.3846*) for all the investigated samples, which is greater than its ideal value of $u = 0.375$ [1], indicates the presence of some deviation from the ideal spinel structure, gives information about oxygen distortion in the structure, and its enhancement suggests higher structural disorder.

Table 3.

Variation of u with δ (Figure 4a) depicts a linear decrease of Oxygen positional parameter u, with inversion parameter, expressed by following experimental equation: $u = 0.36 - 0.007\,\delta$. Figure

4 (b) illustrates ion irradiation dependence of bond angles ($\theta_1, \theta_2, \theta_3, \theta_4, \theta_5$), provides information on A-O-A, A-O-B, B-O-B super-exchange interaction [1]. A perusal of Figure 4 (a) depicts that with increasing irradiation dose, a gradual increase of $\theta_1, \theta_2, \theta_5$ with the concurrent decrease of θ_3, θ_4 suggests, the strengthening of A-O-B, A-O-A super-exchange interaction weakening of B–O–B interaction. The observed modification will have an effect on magnetic properties, as was also observed earlier in [6, 16, 30].

Figure 4.

Table 4 depicts the irradiation-dose dependence of magnetic parameters: experimental ($M_{s(exp.)}$) ; theoretical saturation magnetization $M_{s(th.)}$), coercivity (H_c), magnetocrystalline anisotropy (K_1), remanence (M_r) squareness ratio (M_r/M_s), and dead layer thickness (t). A perusal of Table 4 depicts the reduction of $M_{s(exp.)}$ with increasing ion irradiation, which is consistent with the increase of dead layer thickness (t) [31], leading to a reduction of $M_{s(exp.)}$, attributed to irradiation-induced spin disorder at the surface of the particle, as described earlier [16, 20]. Obtained M_r/M_s is ~ 0.07, indicates dissimilarity of inter-grain interaction, and isotropic behavior of multi-domain grains, as described in [32, 33, 34], with no preferential magnetization direction is consistent with the literature [16, 35].

Table 4

The effect of ion irradiation on hysteresis loops of the studied samples is shown in Figure 5 (a), while the inset of Figure 5(a) shows expanded view of M-H curves, showing coercivity, and its variation with ion irradiation. Figure 5 (b) depicts a variation of $M_{s(exp.)}$ and $M_{s(th.)}$ with irradiation dose, non-similar trend governed by three sub-lattice mode [36, 37], shown by non-zero canting angles given in Table 4. Figure 5 (b) (inset) shows dependence of $M_{s(exp.)}$, $M_{s(th.)}$ on oxygen positional parameter (u), and the increase of the magnetization ($M_{s(exp.)}$, $M_{s(th.)}$), which is attributable to increase of disorder [16, 20].

Figure 5

Figure 6 (a) shows the dependence of K_1 with irradiation dose, and reveals that within experimental errors K_1 does not change much, described by experimental relation: $K_1 = 2.41 - 0.83$ *[Irrr. dose]*. Figure 6 (b) illustrates the irradiation dose dependence of coercivity (H_c). The observed behaviour of H_c with irradiation dose is consistent with obtained strain *(ε)*, and *u* parameter as described in earlier works [16, 20]. Inset of Figure 6 (b) shows the linear dependence of coercivity (H_c) on dislocation density (ρ_D), described by the following experimental relation*:* $H_c = 41.79 + 0.58$ *[ρ_D]*. Higher ρ_D leads to increased hindrance domain wall motion. Thus, the Hc is increased [38].

Figure 6

Figure 7 (b) left panel (hysteresis loops) and corresponding first derivative dM/dH (right panel), shows double peak behaviour and describes the competition between exchange coupling, and strong dipolar interaction [39, 40]. Broader peaks indicate nanocrystalline samples containing dislocations and defects in the crystal [41]. Peak broadness is also linked with the stability of the material: broader the peak of first derivative, the more stable is the structure of the nanoparticle [42].

Figure 7

Table 5 depicts the irradiation dose dependence of full width at half maxima (FWHM) of 1st derivative peak, switching field distribution (SFD), and peak height of 1st derivative. Perusal of Table 5 shows that for the peak height varies between 3.27 – 136.47, as was also observed in [41]. An increase of d*M* / d*H* peak height indicates that the studied samples have a good magnetic state of crystalline cubic spinel structure [33].

Table 5

A perusal of Table 5, the full width at half maxima (FWHM) of 1st derivative (ranges between 7.75 and 513.32). Lower FWHM values suggest uniform particle size [43] and irradiation-induced variation of FWHM indicates modification of particle size, as can also be seen in Table 2. Switching field distribution '*SFD*' is an important magnetic parameter and it measures the energy barrier distribution in a nanoparticle system, and is accompanied by a distribution of particle coercivity [33, 42, 44]. Systems with small *SFD* and high H_c are appropriate for high-density recording [45], and the

smaller the distribution of the switching field, the better is the performance of magnetic recording materials. For the studied samples the SFD range is between 0.17 and 11.72. Thus, among the studied samples: i) the samples irradiated with 1×10^{12} (ions/cm^2), lowest *SFD* (0.17), and highest H_c (44.72 Oe) show potential application in magnetic recording, and ii) 1×10^{13} (ions/cm^2) irradiated sample with lowest H_c (42.63 Oe), highest *SFD* (11.72), would be of use for targeted drug delivery applications [43]. Switching field distribution '*SFD*' values have a strong relation with the particle size distribution because particles with different sizes and shapes will tend to reverse at different magnetic field strengths. Consequently, in studied samples, the observed variation of *SFD* values is ascribable to the variation of the particle size distribution [42].

The irradiation causes the formation of donor and acceptor active centers on the ferrites' surface. Antistructural modeling is used to describe the active centers formed on the zinc ferrite surface. Combining the crystal-chemical composition with spinel antistructure $V_A^{''}\left[V_2^{'''}\right]_B(V_4^{\bullet\bullet})_O$ allows seeing the ions with excessive charge in the spinel lattice:

$$\left(Zn_{1-x}^{2+}Fe_x^{3+}\right)_A\left[Zn_x^{2+}Fe_{2-x}^{3+}\right]_B\left(O_4^{2-}\right)_O+V_A^{''}\left[V_2^{'''}\right]_B(V_4^{\bullet\bullet})_O\rightarrow (Zn_{1-x}^{\times}Fe_x^{\bullet})_A\left[Zn_x^{'}Fe_{2-x}^{\times}\right]_B(O_4^{\times})_O$$

where ● is an excess of the positive charge, ' is an excess of the negative charge, × is an effective zero charge; the x value changes from 0.20 (for pristine sample) to 0.15, 0.21, 0.30 (for samples irradiated at 1×10^{11}, 1×10^{12} and 1×10^{13} ions/cm^2 respectively). It can be seen that the concentration of positively charged ferric ions $Fe_A^{\bullet}$ in A-sites and negatively charged zinc ions $Zn_B^{'}$ in octahedral (*B*) sites increases with an increase in irradiation dose. Therefore, the irradiated samples will be more active in the catalytic or other processes in comparison with the pristine sample due to the presence of a higher amount of surface-active centers.

4. Conclusions

To summarize, XRD analysis confirmed the formation of a single-phase nanocrystalline cubic spinel phase. Irradiation results in the alteration of lattice parameters, cationic distribution, disorder, and

dislocation density, which in turn affects A-O-B, A-O-A, and B–O–B super-exchange interaction. Irradiation-induced structural changes noticeably affect the dead-layer thickness, thus affecting saturation magnetization. Magnetization derivative with field (*dM/dH*) suggests the presence of large number of dislocations and proposes applications in high-density recording, and in targeted drug delivery. Antistructural modelling for Zn ferrites describes the surface-active centres. Present studies demonstrate the effectiveness of ion irradiation-assisted tuning of magnetic properties of spinel ferrites.

Acknowledgments: Authors thank Dr. M. Gupta UGC-DAE CSR, Indore, for XRD measurements. SNK acknowledges gratefully for one month of "*Invited Professor*" stay at ENS Paris-Saclay, Cachan (France). This work is supported by Seed money grant: No. Dev/Seedmoney2.0/2020-21/649, 20 Jan. 2022 of Devi Ahilya University, Indore (India). TT thanks the Ministry of Education and Science of Ukraine (project number 0121U109476) for financial support.

References:

1. J. Smit, and H. P. J. Wijn, *Ferrite*, (Philips' Technical Library, Eindhoven, Holland, 1959).
2. M. A. Willard, L. K. Kurihara, E. E. Carpenter, S. Calvin, V. G. Harris, *Int. Mater. Rev.* **49** (3-4), 125 (2004). doi:10.1179/095066004225021882
3. S. S. Mathew , R. S. Juang, *Chemical Engineering Journal* **129** (1-3) , 51 (2007) doi:10.1016/j.cej.2006.11.001
4. K. E. Scarberry et al., *J. Am. Chem. Soc.* **130** (31), 10258 (2008). doi:10.1021/ja801969b
5. M. Sugimato, *J. Am. Ceram. Soc.* **82** (2), 269 (1999). doi:10.1111/j.1551-2916.1999.tb20058.x
6. M. Satalkar et al., *Nucl. Instr. Meth. Phys. Res. B* **379**, 235 (2016). doi: 10.1016/j.nimb.2016.03.052
7. B. Kaur, M. Bhat et al., *J. Magn. Magn. Mater.***305** (2), 392 (2006). doi:10.1016/j.jmmm.2006.01.110
8. D.K. Avasthi, and G. K. Mehta, *Swift Heavy Ions for Materials Engineering and Nanostructuring*, (Springer series, 2011).
9. I.P. Jain, and G. Agarwal, Ion beam induced surface and interface engineering, *Surf. Sci. Rep.* **66** (3-4), 77 (2011). doi:10.1016/j.surfrep.2010.11.001
10. J.P. Singh et al., *J. Magn. Magn. Mater.* **324** (20), 3306 (2012). doi:10.1016/j.jmmm.2012.05.039
11. X. Wang et al., *Appl. Phys. Rev.***7** (4), 041303 (2020). doi: 10.1063/5.0021322
12. R. Kumar et al., *Radiat. Eff. Defects Solids* **147**(3), 187 (1999). doi: 10.1080/10420159908229008
13. M. Toulemonde, *Nucl. Instrum. Methods B* **156** (1–4), 1 (1999). doi: 10.1016/S0168-583X(99)00287-6
14. L. Raghavan et al., *Nucl. Instr. Meth. Phys. Res. B* **396**, 68 (2017). doi: 10.1016/j.nimb.2017.01.046

15. J. P. Singh et al., ***Phys. Chem. Chem. Phys.*** **20 (17),** 12084 (2018). doi: doi.org/10.1039/C8CP00368H
16. C. Parmar et al., *J. Solid state science and tech.* **11**, 0530150 (2022). doi: 10.1149/2162-8777/ac6f1b
17. R. Sharma et al., *AIP Conf. Proc.* **1953** (1), 030117 (2018). doi: 10.1063/1.5032452
18. S.N. Dolia et al., *Radiat. Eff. Defects Solids* **166** (8-9), 558 (2011). doi: 10.1080/10420150.2011.553232
19. J.P. Singh et al., *Current Appl. Phys.***11**(3), 532 (2011). doi:10.1016/j.cap.2010.09.009
20. S. Raghuvanshi et al., *J. Magn. Magn. Mater.***471**, 521 (2019). doi: 10.1016/j.jmmm.2018.10.004
21. J.F. Ziegler, J.P. Biersack, and U. Littmark, Pergamon, *The Stopping and Range of Ions in Matter*, (Treatise on Heavy-Ion Science, Springer, New York, 1985). doi: 10.1007/978-1-4615-8103-1_3
22. L. Lutterotti, and P. Scardi, *J. Appl. Cryst.***23**(4),246(1990). doi: 10.1107/S0021889890002382
23. R. Verma et al., *Mater. Today: Proc.***46**,2205 (2021). doi: 10.1016/j.matpr.2021.03.204
24. R. S. Yadav et al., *Adv. Nat. Sci.: Nanosci. Nanotechnol.***8** (4), 045002-1 (2017). doi:10.1088/2043-6254/aa853a
25. C. Parmar et al., *AIP Conference Proceedings* **2142** (1), 160014 (2019). doi: 10.1063/1.5122595
26. E. F. Bertaut, and C. R. Hebdomadaires, *des Séances de l'Academie des Sciences* **230**, 213 (1950).
27. A. R. Tann, H. H. Joshi, World Academy of Science, Engineering and Technology, International Journal of Physical and Mathematical Sciences 7 (3), 334 (2013). doi.org/10.5281/zenodo.1333917
28. P. Chen et al., *Phy. Rev. B***54**(13), 9288 (1996). doi:10.1103/physrevb.54.9288
29. Y. Yafet, and C. Kittel, *Phys. Rev.* **87** (2), 290 (1952). doi:10.1103/PhysRev.87.290
30. M. Satalkar, S. N. Kane, and S. Raghuvanshi, *AIP Conf. Proc.***1953**, 030069 (2018). doi: 10.1063/1.5032404
31. J. M. D. Coey, *Phys. Rev. Lett.***27** (17) 1140 (1971). doi: 10.1103/PhysRevLett.27.1140

32. E. C. Stone,r and E. P. Wohlfarth, *Philos Trans R Soc London A* **240** (826), 599 (1948). doi: 10.1098/rsta.1948.0007

33. I. P. Muthuselvam, and R. N. Bhowmik, *J Magn. Magn. Mater.* **322** (7), 767 (2010). doi:10.1016/j.jmmm.2009.10.057

34. E. Tirosh, G. Shemer, and G. Markovich, *Chem Mater***18** (2), 465 (2006). doi: 10.1021/cm052401p

35. S. N. Kane, and M. Satalkar, *J. Mater. Sci.* **52** (), 3467 (2017). doi: 10.1007/s10853-016-0636-7

36. S.N. Kane et al., *Mater. Today: Proc.* **32** (3), 358 (2020). doi:10.1016/j.matpr.2020.02.036

37. N. S. S.Murthy et al., *Phys. Rev.* **181** (2), 969 (1969). doi:10.1103/PhysRev.181.969

38. A. K. Lindquist et al., *Earth, Planets and Space* **71** (5), 1 (2019). doi:10.1186/s40623-018-0981-7

39. A. G. Kolhatkar et al *Int. J. Mol. Sci.* ***14***, 15977 (2013) doi:10.3390/ijms140815977

40. E. E. Ateia et al, *J Mater Sci: Mater Electron* **33**, 8958 (2022). doi: 10.1007/s10854-021-07008-9

41. T. Dippong et al *Nanomaterials* **10,** 580-1 (2020). doi: 10.3390/nano10030580

42. S. Kumar et al, *Mater. Sci. Eng.* **B 272**, 115362-1 (2021). Doi: 10.1016/j.mseb.2021.115362

43. S. Kumar et al, *Journal of Inorganic and Organometallic Polymers and Materials*, **31**, 528 (2021). doi: 10.1007/s10904-020-01764-7

44. D. Jiles , *Introduction to Magnetism and Magnetic Materials* (Chapman and Hall), New York, 1991). DOI 10.1007/978-1-4615-3868-4

45. J. C. Lodder, Handbook of Magnetic Materials , chapter 2, Magnetic recording hard disk thin film media, in Handbook of Magnetic Materials, **11** 291(1998). Doi:10.1016/S1567-2719(98)11006-5

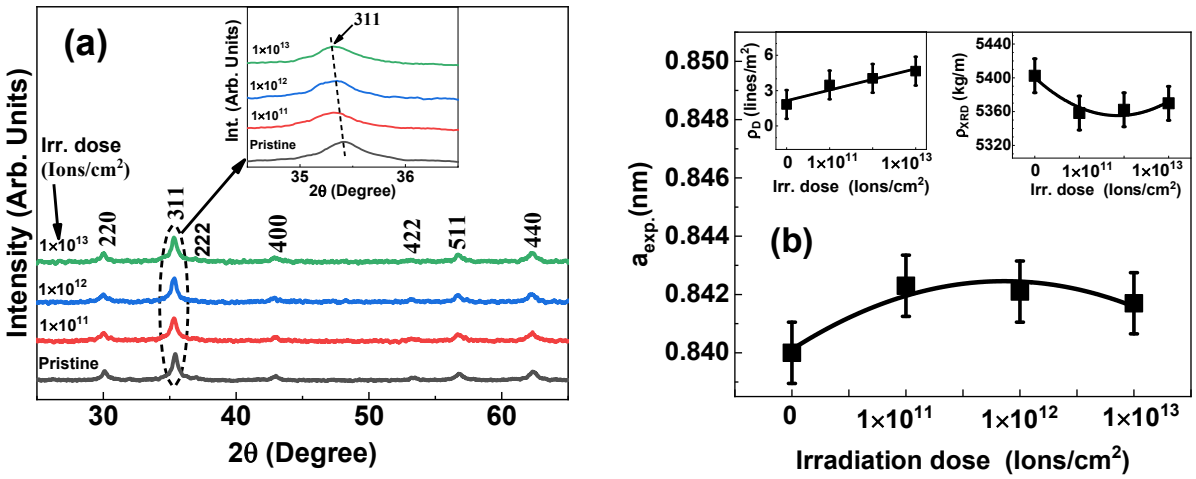

Figure 1. **(a)** XRD patterns of Pristine, and ion-irradiated (dose: 1×10^{11} ions/cm^2, 1×10^{12} ions/cm^2, 1×10^{13} ions/cm^2) samples (**inset**: expanded view of (311) peak); **(b)** $a_{exp.}$ dependence with ion flounce, and line connecting points is a polynomial fit to the experimental data. **Inset:** irradiation dose dependence of ρ_{XRD} (**Right inset)**, and ρ_D (**Left inset)**. Line connecting points in the left inset of Fig. (b) is a guide to the eye.

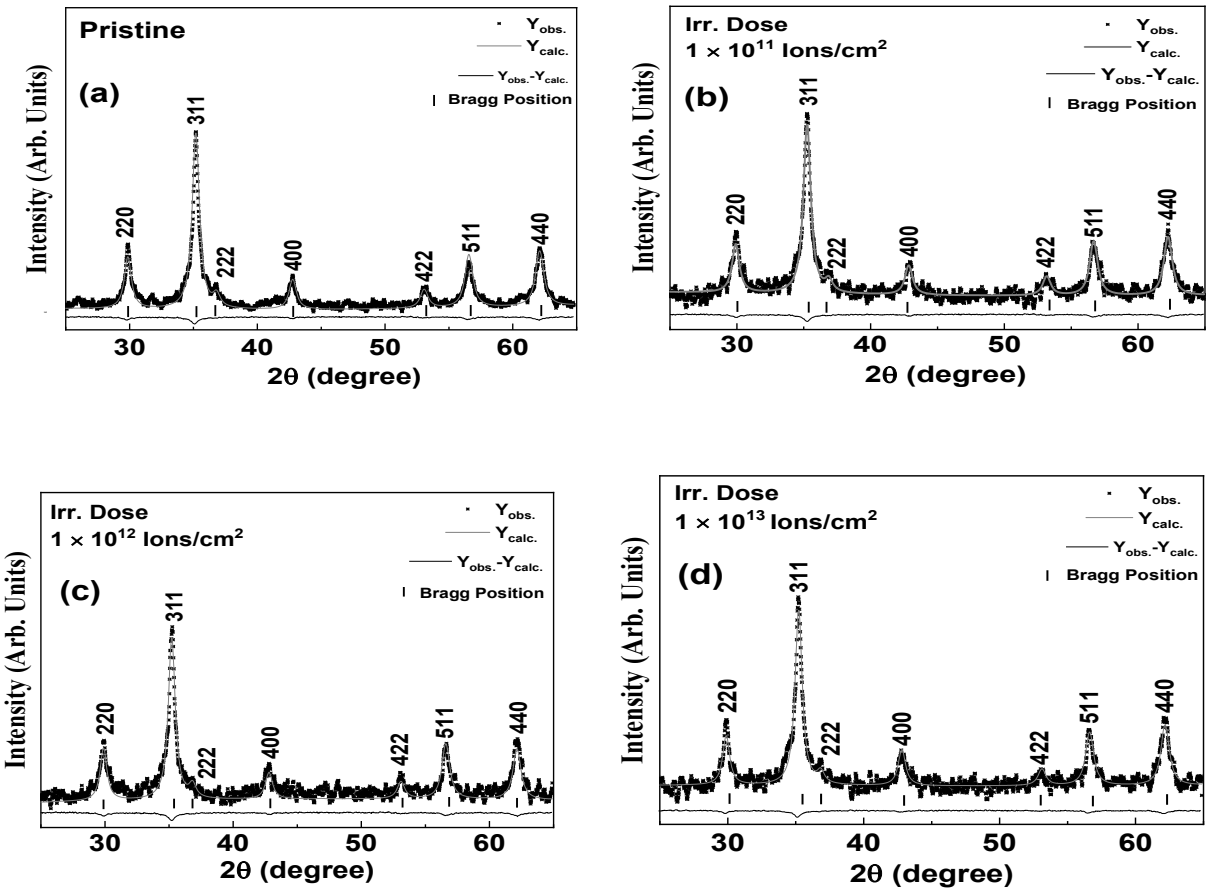

Figure 2: Rietveld refined XRD patterns of pristine and irradiated samples.

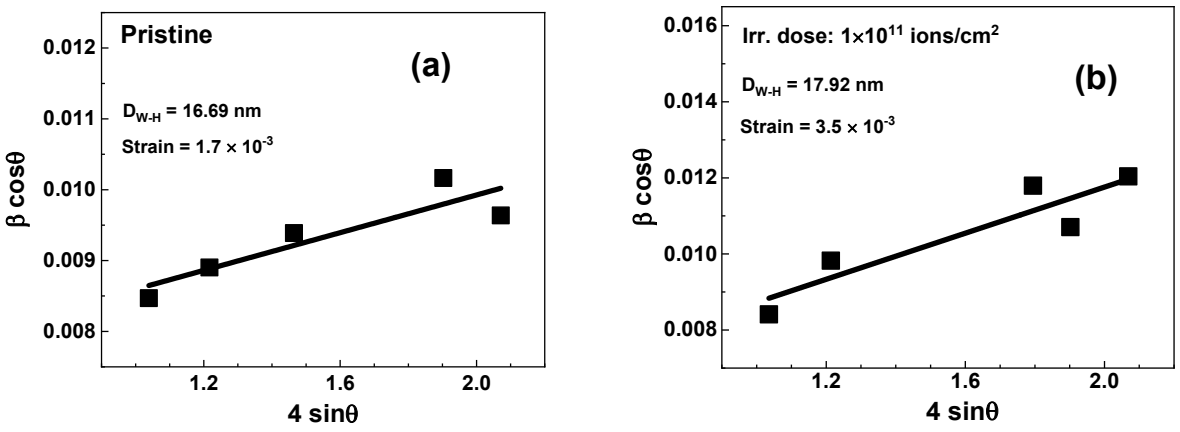

Figure 3: Representative W−H plot for (a) pristine and (b) irradiated sample (*dose: 1 × 10^{11} Ions/cm^2*).

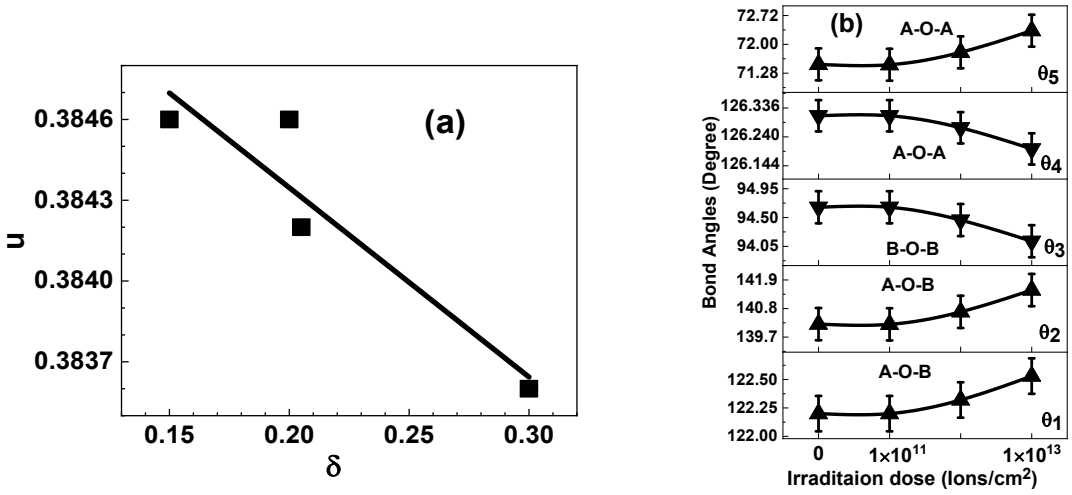

Figure 4: **(a)** Bond angle variation with ion flounce, **(b)** Variation of oxygen parameter *(u)* with inversion parameter *(δ)*.

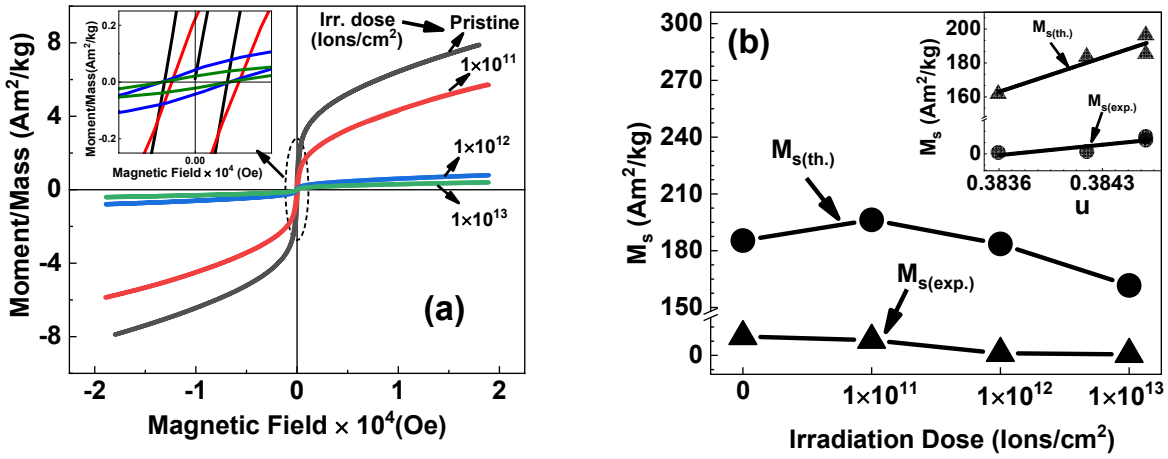

Figure 5: (a) M-H curves for pristine and irradiated samples. *Upper inset:* expanded view of M-H curves showing coercivity, and its variation with ion flounce. **(b)** $M_{s(exp.)}$ dependence with irradiation dose, *inset: u* dependence of $M_{s(exp.)}$, $M_{s(th.)}$. Line connecting points in Fig. 5(b) are guides to the eye.

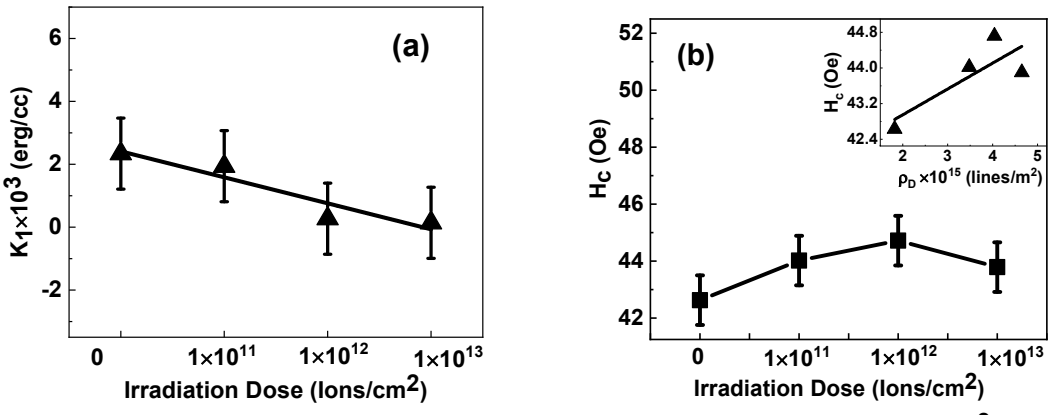

Figure 6. Irradiation dose dependence of (a) anisotropy and (b) coercivity (H_c). *Inset:* variation of H_c with ρ_D.

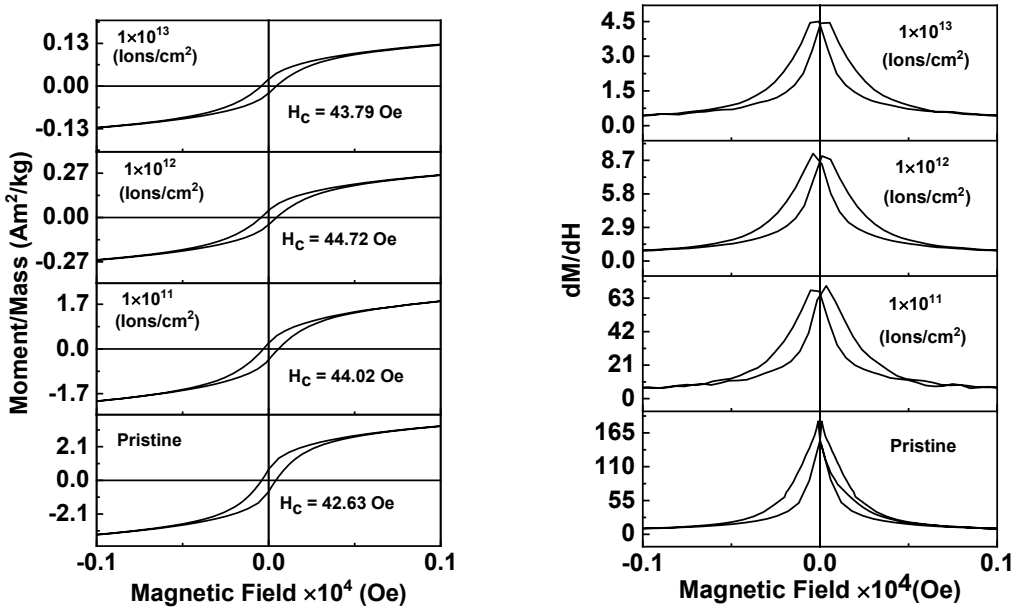

Figure 7. First derivative of magnetization dM/dH. Hysteresis loops (left panel), and corresponding first derivative of magnetization 'dM/dH' (right panel).

Table 1. Reitveld refined R-parameters (R_{wp}, R_p, $R_{exp.}$), Shape parameters (u, v, w), the goodness of fit (GOF) for pristine, irradiated samples

Irradiation dose (ions/cm^2)	**R_{wp}**	**R_p**	**R_{exp}**	**GOF**	**u**	**v**	**w**
0	20.9	18.21	10.25	2.03	0.001	-0.004	0.015
1×10^{11}	1.29	1.27	3.94	0.4	-0.025	-0.012	0.013
1×10^{12}	30.43	26.64	14.07	2.16	0.003	-0.041	0.002
1×10^{13}	1.65	1.31	3.82	0.43	0.002	0.003	-0.002

Table 2. Irradiation dose dependence of theoretical and experimental lattice parameter ($a_{th.}$, $a_{exp.}$), Williamson Hall (W-H) grain diameter (D_{W-H}), x-ray density (ρ_{xrd}), cell volume (V), strain (ε), and dislocation density (ρ_D) for the $ZnFe_2O_4$ samples

Irradiation dose (ions/cm^2)	a_{exp} **(nm)** (±0.0011)	a_{th} **(nm)** (±0.0003)	D_{W-H} **(nm)** (±3.96)	ρ_{xrd} **(kg/m^3)** (±20.09)	**V (nm^3)** (±0.0022)	***S*** **(m^2/g)** (±26.75)	***Strain*** ε (±0.0009)	$\rho_D \times 10^{15}$ ***(Lines/m^2)*** (±1.22 × 10^{15})
0	0.8400	0.8440	16.69	5402.44	0.5927	66.54	0.0017	1.82
1×10^{11}	0.8423	0.8442	17.92	5358.31	0.5976	62.49	0.0035	3.48
1×10^{12}	0.8421	0.8439	9.25	5362.13	0.5972	120.9	0.0021	4.04
1×10^{13}	0.8417	0.8435	12.63	5369.78	0.5963	88.47	0.0033	4.65

Table 3. Irradiation dose dependence of the cationic distribution (for ***A*** and ***B-site***), oxygen positional parameter (***u***), inversion parameter (***δ***), and canting angle ($\alpha_{Y\text{-}K}$), and intensity ratios of $\mathbf{I_{400}/I_{422}}$, $\mathbf{I_{220}/I_{440}}$ for $ZnFe_2O_4$ samples.

Irr. dose	**Cation Distribution**		***u***	***δ***	$\alpha_{Y\text{-}K}$ (°)	I_{400}/I_{422}		I_{220}/I_{440}	
(Ions/cm²)	**A site**	**B site**	(±0.0005)	(±0.06)	(±1.74)	**Calc.**	**Obs.**	**Calc.**	**Obs.**
0	$(Zn^{2+}_{0.80}Fe^{3+}_{0.20})$	$[Zn^{2+}_{0.20}Fe^{3+}_{1.80}]$	0.3846	0.20	80.86	1.4962	1.5213	0.9337	1.0684
1×10^{11}	$(Zn^{2+}_{0.85}Fe^{3+}_{0.15})$	$[Zn^{2+}_{0.15}Fe^{3+}_{1.85}]$	0.3846	0.15	83.19	1.1012	1.0876	0.8942	0.9211
1×10^{12}	$(Zn^{2+}_{0.79}Fe^{3+}_{0.21})$	$[Zn^{2+}_{0.21}Fe^{3+}_{1.79}]$	0.3842	0.21	83.14	1.3857	1.3667	0.8717	0.9191
1×10^{13}	$(Zn^{2+}_{0.70}Fe^{3+}_{0.30})$	$[Zn^{2+}_{0.30}Fe^{3+}_{1.70}]$	0.3836	0.30	79.67	1.2153	1.1585	0.8602	0.9165

Table 4. Variation of magnetic parameters (at 300 K): saturation magnetization ($\mathbf{M_{s(exp.)}}$), coercivity ($\mathbf{H_c}$), anisotropy ($\mathbf{K_1}$), retentivity ($\mathbf{M_r}$), squareness ratio (M_r/M_s), and deadlayer thickness with irradiation doses of O^{6+} on $ZnFe_2O_4$.

Irradiation dose (Ions/cm^2)	**$M_{s(exp.)}$ (Am^2/kg)** (±4.78)	**$M_{s(th.)}$ (Am^2/kg)** (±14.51)	**H_c (Oe)** (±0.87)	**$K_1 \times 10^3$ (erg/cc)** (±1.13)	**M_r (Am^2/kg)** (±0.3116)	**M_r/M_s** (±0.0153)	**t (nm)** (±0.41)
0	9.96	185.34	42.63	2.34	0.6890	0.0692	2.21
1×10^{11}	8.05	196.27	44.02	1.94	0.3163	0.0392	2.49
1×10^{12}	1.10	183.57	44.72	0.27	0.0427	0.0399	1.51
1×10^{13}	0.57	161.63	43.90	0.14	0.0211	0.0370	2.08

Table 5. Irradiation dose dependence of coercivity (**H_c**), full width at half maxima (**FWHM**) of 1st derivative peak, switching field distribution (SFD), and a peak height of 1st derivative.

Irradiation dose (ions/cm^2)	H_c (Oe)	FWHM or ΔH of 1st derivative peak (Oe)	SFD ($\Delta H / H_C$)	Peak Height of 1st derivative
0	42.63	325.37	7.63	136.47
1×10^{11}	44.02	504.60	11.46	50.31
1×10^{12}	44.72	7.75	0.17	18.94
1×10^{13}	43.79	513.32	11.72	3.27

Figure captions

Figure 1. **(a)** XRD patterns of Pristine, and ion-irradiated (dose: 1×10^{11} ions/cm^2, 1×10^{12} ions/cm^2, 1×10^{13} ions/cm^2) samples (**inset**: expanded view of 311 peak); **(b)** $a_{exp.}$ dependence with ion flounce, and line connecting points is polynomial fit to the experimental data. **Inset:** irradiation dose dependence of ρ_{XRD} (**Right inset)**, and ρ_D (**Left inset)**. Line connecting points in left inset of fig. (b) is guide to the eye.

Figure 2: Reitveld refined XRD patterns of Pristine, and irradiated samples.

Figure 3: Representative W–H plot for (a) Pristine, and (b) irradiated sample (*dose: 1 × 10^{11} Ions/cm^2*).

Figure 4: **(a)**Bond angle variation with ion flounce,**(b)**Variation of oxygen parameter *(u)* with inversion parameter *(δ)*.

Figure 5: (a) M-H curves for pristine, and irradiated samples. *Upper inset:* expanded view of M-H curves showing coercivity, and its variation with ion flounce.**(b)**$M_{s(exp.)}$dependence with irradiation dose, *inset:u* dependence of $M_{s(exp.)}$, $M_{s(th.)}$. Line connecting points in fig. 5(b) are guide to the eye.